



Understanding the bonding mechanism in short-time resistance projection welding: a comprehensive analysis

Johannes Koal¹ · Martin Baumgarten¹ · Jörg Zschetzsche¹ · Hans Christian Schmale¹

Received: 8 August 2023 / Accepted: 20 December 2023 / Published online: 16 January 2024
© The Author(s) 2024

Abstract

Capacitor discharge welding (CDW) is characterized by a pulsed electrical current profile. It is primarily utilized for resistance projection welding tasks, offering high power densities and short welding times. According to the latest findings, the welding process can be divided into different phases: contacting, activating, material connection, and holding pressure. During the activation phase, high-speed video-imaging reveals the generation of metal vapor which effectively eliminates impurities and oxide layers from the contact zone. The result of this is an activated surface. The purpose of this paper is to describe the physical effects of the bonding mechanism during short-time resistance welding. The Chair of Joining Technology and Assembly at the Technische Universität Dresden has a laboratory facility that can interrupt the welding current at any desired time during capacitor discharge welding. This allows different welding current profiles with always the same current rise time to be scientifically investigated. The experimental findings were supplemented with simulative analyses to clarify the bonding mechanism in resistance projection welding. Three different surface conditions are considered to generalize the findings on the bonding mechanism. Temperature and current density distributions were assessed to provide a physical description of the activation phase. The power density in the joining zone at different interruption times is determined, which gives an indication of activation by metal vaporization. The material connection is determined experimentally for the same interruption times. The numerical simulation model can be used to describe the bonding mechanism in short-time resistance welding. In resistance welding, the bond is formed due to the molten phase (solidification structure). In short-time resistance welding, the bond is formed due to surface activation by metal vaporization.

Keywords Bonding mechanism · Resistance welding · Short-time welding · Numerical simulation · Capacitor discharge welding

1 Introduction

A welded joint is a connection of the same type and material. It is based on the interaction of atomic forces in the joint. The requirement is that the surfaces are free of contamination and oxides (activated) and have a small atomic distance (order of magnitude 10^{-10} m = 0.1 nm) [1–6]. The power density is essential for the characteristics of the welding process when the joint is thermally established. If the power density is

too low, most of the thermal energy is transferred by thermal conduction into the base material, the apparatus and the electrodes without a joint being formed. If the power density is high enough, the material is locally melted. If the power density is further increased, the material is locally vaporized (see Fig. 1).

The material connection is established in the liquid state by mixing of molten materials and following solidification or in the plastic state by removing the foreign layers from the surface (activation) and bringing the surfaces closer together by local plastic deformation of the component. The welded joint is mostly formed via the liquid state. In this case, a solidified structure is formed after welding, which differs from the base material produced by rolling and which is clearly visible in the microstructure. This mechanism is basically required

✉ Johannes Koal
johannes.koal@tu-dresden.de

¹ Technische Universität Dresden, Institute of Manufacturing Science and Engineering, Chair of Joining Technology and Assembly, Dresden, Germany

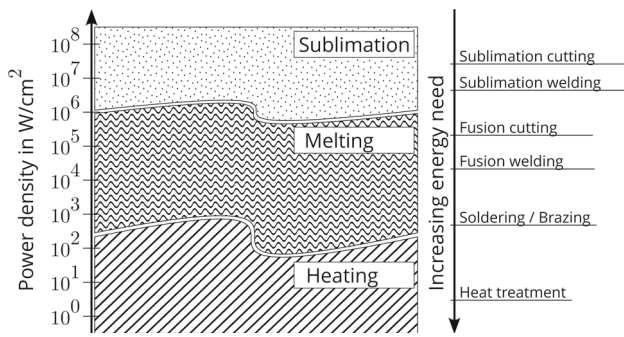


Fig. 1 Classification of power density according to heating, melting, and sublimation. The classification depends on the material, which is why the boundaries vary. So on the abscissa is the influence of the material

for resistance pressure welding as well and provides the basis for evaluating the quality of the welded joint. The weld lens in the cross-section of resistance pressure welded joints is measured and evaluated. This does not absolutely apply to projection welded joints produced by capacitor discharge [7].

There are numerous welded joints that are produced without melting in a plastic state. The most extreme case is cold pressure welded joints, which are produced without additional heat input during very strong plastic deformation [1–6]. The deformation creates the conditions for material bonding by enlarging (activating) the surfaces to at least three times their original size under oxygen exclusion and approximating them to atomic spacing.

Resistance pressure welding requires low deformation degrees. The surface activation in the joining zone can therefore not be achieved by increasing the surface area in the cold state. Surface activation could be observed in high-speed images of past investigations, which can be explained by metal vaporization [7, 8]. The aim of this publication is to use experimental and simulative investigations to describe the bonding mechanism in projection welding by capacitor discharge. This allows a recommendation as to how short-time processes in resistance welding differ from more conventional processes to be made.

2 Process fundamentals

2.1 Projection welding using capacitor discharge

Capacitor discharge welding (CDW or CD-Welding) is a stable, efficient, cost-effective, and easy-to-use joining process. It is mostly used for projection welding. For example, high-strength steels, mixed compounds, coated surfaces, or components with projection diameters up to 200mm can be welded in a few milliseconds [7, 9–13]. Before starting the welding process, one or more capacitor banks are charged.

This causes an electrical energy E_{el} to be stored in the capacitor as a function of the charging voltage U_C and the capacity C (see Eq. 1).

$$E_{el} = \frac{1}{2} C \cdot U_C \quad (1)$$

Discharging the electrical energy E_{el} starts the welding process. The current flow is transferred to the joining point. This results in the transformed and unregulated welding current as shown in Fig. 2. The peak current I_p is reached in a few milliseconds. This time is called the current rise time t_p . The welding time t_h is reached when the peak current I_p drops by 50%. The current flow time t_l is reached when the current drops to 95%.

The characteristic process values of CD welding (see Fig. 2) illustrate the differences to spot welding with medium frequency (MFDC): very high current intensities are obtained in very short current rise times. The projection geometry in the joining zone focuses the current flow and; therefore, increases the electric current density j . The amount of heat Q is generated in an electrical wire as a function of the square of the current and the ohmic resistance R , based on Joule's heat law (see Eq. 2). In Eq. 3, is the differential observation for the local description of the heating by the heat flux density \dot{q} . This depends on the specific electric resistance ρ of the material and the current density j . That shows that a high current density in the joining zone results in a high heat flux density. The high power density in the joining area is the critical parameter for the heating of the short-time projection welding process. The heat flux \dot{Q}_W caused by the resistance heating in the projection and component is much smaller than the heat flux \dot{Q}_R caused by the contact resistance heating in the joining zone at the beginning of the process (see Eq. 4). As a result, no nugget diameter is obtained in CD projection welding (see Fig. 3).

$$Q = I^2 \cdot R \cdot t \quad (2)$$

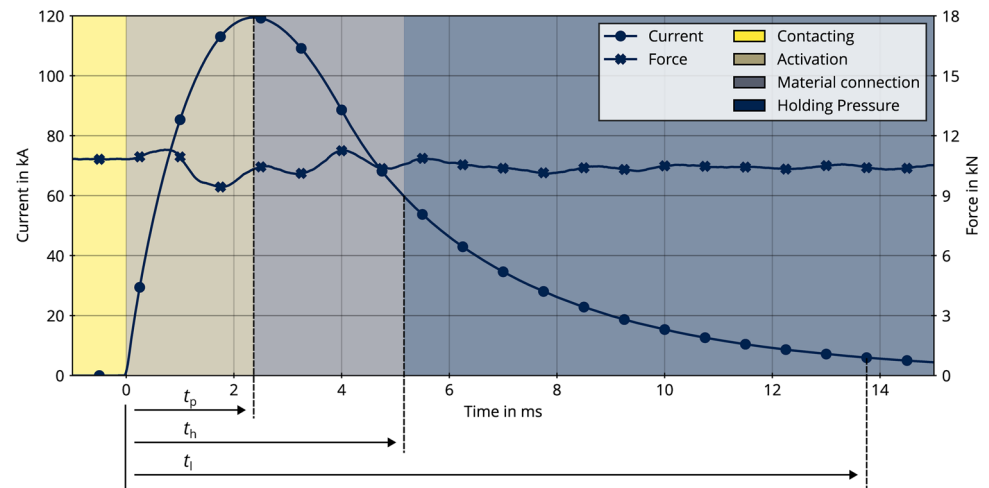
$$\dot{q} = \frac{\dot{Q}}{V} = \rho \cdot j^2 \quad (3)$$

$$\dot{Q}_R = \iint j^2 \cdot R_C \cdot dA \gg \dot{Q}_W = \iiint I^2 \cdot R \cdot dV \quad (4)$$

2.2 Short-time welding with high heat flux

Short-time welding processes in resistance pressure welding are characterized by the fact that the connection is not formed via the molten phase, but by activating the surfaces through metal vaporization and subsequently pressing them together [7, 8, 14]. High power densities are required to

Fig. 2 Characteristic of the current curve by capacitor discharge projection welding and schematic procedure for short-time welding



achieve metal vaporization in the joining zone. Laser key-hole welding involves the formation of a keyhole within a metal by vaporization when high power densities are attained. Recent research indicates that these power density requirements range from 1 MW/cm^2 to 5 MW/cm^2 [15–17]. To achieve a high power density ($\geq 1 \text{ MW/cm}^2$ for the activation of the surface, very high current gradients are required, which leads to very short welding times. Therefore, there is no solidification structure and no nugget in the joint (see Fig. 3). Measuring a solidification structure (weld or nugget diameter) as a quality assessment is therefore not permitted for short-time welding processes. The process occurs in four characteristic phases that smoothly flow into each other (see Fig. 2) [8, 18]:

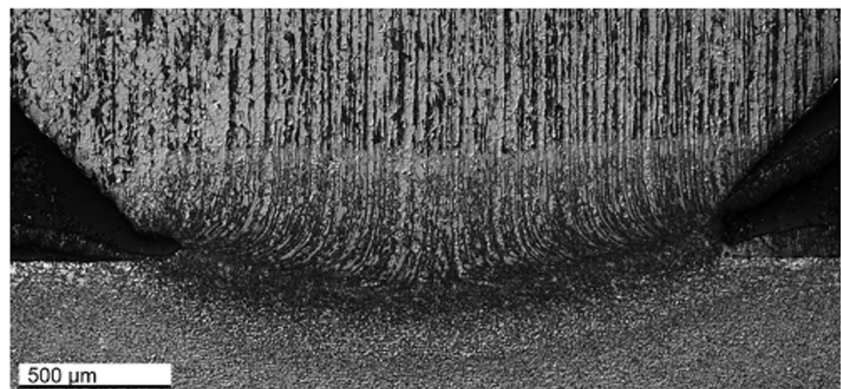
- 1. Contacting**, characterized by the movement and contacting of the electrodes, the increase of the electrode force up to the welding force (force buildup) and the formation of the contact area. Locally different surface pressures and relative movements of different magnitudes lead to locally characterized contact resistances.
- 2. Activation**, characterized by the current flow with a very high current gradient and very high power density in

the contact area. Metal vaporization occurs in the contact zone. Foreign and oxide layers are carried away with the expanding metal vapor and the surface is activated as a result. The current density is not constant in the entire contact area. The power density is greater at the edge due to the geometric constriction of the current path. Metal vaporization occurs there first. The contact area where metal vapor is present is no longer electrically conductive. The current flows over the remaining contact area, which is then also successively activated by metal vaporization. The electrodes are not followed up during this phase.

3. Material connection, characterized by the beginning of the settling of the electrodes, pressing the activated surfaces onto each other, establishing the material connection and removing the contact resistance, decreasing current intensity and current density, decreasing metal vaporization and the beginning of plastic deformation of the joining area.

4. Holding pressure, characterized by the follow-up of the electrodes, further decrease of the current flow, plastic deformation of the joining zone and establishment of the material connection in non-activated areas (should melt

Fig. 3 Joining zone during CD projection welding without nugget and a solidification structure



be formed, it is pressed out of the joining zone), increase of the bonding area, end of the follow-up of the electrode, thermal conduction, and cooling of the joining zone.

The process procedure is typical for projection welding with capacitor discharge. However, the required current strengths with very low current rise times can also be achieved with other current sources, e.g., medium-frequency systems.

2.3 Numerical simulation of projection welding

The welded joint is established in resistance welding by capacitor discharge:

- by mechanical, thermal, and electrical stress,
- directly (5 to 15 ms),
- covered and
- without formation of a nugget.

Only numerical process simulation can be used to investigate the covered short-time welding process, because the FEM allows a:

- mechanical, thermal and electrical evaluation,
- time resolution of the loads,
- local resolution of the loads,
- sensitivity analyses of different boundary conditions.

The following complexities can be identified for CD projection welding from the process characteristics for modeling purposes:

- high-temperature gradients,
- temperature-dependent deformation of the projection,
- effect of the contact resistance,
- activation by removing the outer boundary layer and
- formation of different phases / temperature-dependent material models.

In [19, 20] the modeling of a static numerical simulation for CD projection welding is described. Balance equations are obtained and implemented by finite element methods. The temperature distribution is evaluated depending on different projection geometries and the mechanical stress at different times. The implementation of the contact resistance is not included. Casalino et al. investigate in [21, 22] the temperature evolution during simultaneous CD welding of multiple projections. An iteratively coupled multiphysics model is developed for this purpose, which is validated by experiments. The purpose of the study is to investigate the effect of projection geometry and to determine welding parameters. The implementation of the contact theory, the plastic

temperature-dependent deformation, and the surface activation are not part of the investigations. These investigations are continued by Cavaliere et al. [23] using a three-dimensional simulation model. The implementation of electrical and thermal conductivity in the contact and the consideration of temperature-dependent flow stress curves is done. Zhu et al. [24] and Sun [25] describe two similar simulation models. The current sources used are medium-frequency direct current sources rather than capacitor discharges. This results in different complexities, since the joining connection is made via the molten phase [25–28]. The contact resistance is [29] implemented and the mechanical and thermal-electrical simulation environments are iteratively coupled. Thereby, Sun states: “It should be mentioned that, because of the large deformation involved in the analyses, it is more difficult to get converged solutions for projection welding than for spot welding [...]” [25, p. 250]. A remeshing is absolutely necessary in projection welding for this reason. Furthermore, the implementation of a contact resistance theory is essential. This is done by Wehle and Long [12, 30]. Hamedi and Atashparva provide in [31] a review paper about different contact theories. Song has investigated a contact resistance theory for projection welding in [32]. This theory is validated for medium-frequency welding, but not for CD welding. The purpose of the simulation model is to take all complexities into consideration. A simulation model was developed at the Technische Universität Dresden that takes into account temperature-dependent material data, a validated contact theory and adaptive remeshing for large projection deformations [14, 18, 33]. This allows to calculate the power density in the joining zone and therefore to evaluate a possible surface activation by metal vaporization.

3 Experimental and numerical procedure

3.1 Experimental investigation

The resistance welding task consists of a sheet and a ring projection with a projection diameter $d = 15$ mm, radial contact area $r = 1$ mm and a projection angle $\alpha = 45^\circ$ (see Fig. 4). The sheet thickness of the component is $t = 3$ mm. The ring projection and the sheet are made of S355MC. The resistance welding electrodes are made of CuCr1Zr. Three different surface conditions of the sheet are investigated in order to obtain a high degree of generality in the experiments:

1. As delivered
2. Grinded
3. Galvanized

The different surface conditions are shown in Fig. 5. A regular rolling skin can be seen in the surface condition: *as*

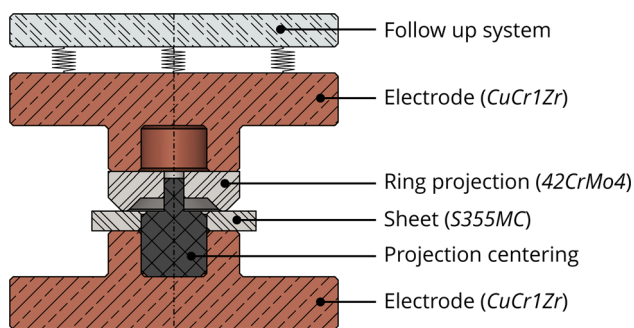


Fig. 4 Schematic resistance welding task with ring projection, sheet, projection centering, welding electrodes, and the follow-up system

delivered. The sheets were grinded in order to evaluate in general the influence of a layer. The zinc layer allows to evaluate the influence of a low-melting layer.

The experimental investigations are performed on a portal system *KKP 18-MCS/gKE* of the company *KAPKON GmbH*. Four capacitor banks are available for capacitor discharge. A peak current up to 210 kA can be realized in 2.1 ms. A unique feature is the process-integrated transition resistance measurement during CD welding. During the transition resistance measurement, the CD circuit is disconnected so that the measurement current flows solely through the welding task. Additionally, the current flow in the welding process can be interrupted. This results in different current profiles, which have different current maxima I_p and current rise times t_p , but always the same current rise rate (current curve to current maximum I_p). The time t at which the current flow is interrupted is defined as the interruption time t_I . This behavior is shown in Fig. 6 for the surface condition *As delivered*.

The outer current curve shows the typical current curve during the complete discharge of the capacitor bank. The inner curves show the current curve with lower peak current I_p and lower current rise time t_p when the capacitor discharge is interrupted early. This is how an interrupted welding pro-

cess is experimentally done. The capacitor bank was charged with a voltage $U_C = 1000$ V. This capacitor bank has a capacity C of 21 320 μF . According to equation Eq. 1 this results in a charging energy of 10.66 kW s. This electrical charging energy E_{el} allows the activation to be investigated since no welding connection is established at an interruption time $t_I = 0.4$ ms and the upper limit of the welding range has been established at an interruption time $t_I = 30$ ms.

The upper limit is defined by the appearance of weld spatter classes 2 to 3, according to [7, 14] and by imperfections in the cross section. A total of 11 interruption times t_I were investigated per surface condition. Each interruption time was repeated 7 times. A static press-out test was performed for each experiment. A total of 230 experiments were evaluated, as one false measurement was removed.

3.2 Numerical investigation

The finite element method (FEM) allows a local and temporal assessment of the mechanical, thermal, and electrical loads. Figure 7 shows a schematic 2D axisymmetric representation of the simulation model with the joining parts, resistance electrodes, contact areas, and boundary conditions. The temperature-dependent material properties and the temperature-dependent flow stress curves are described in [14, 34, 35]. An adaptive remeshing has to be considered to avoid convergence problems because of the strong projection deformations. Because of that, an iteratively coupled simulation model for CD projection welding was developed at the Technische Universität Dresden with *ANSYS MECHANICAL APDL* [14, 18]. The adaptive remeshing is described in detail in [12, 30, 33]. Figure 8 shows the procedure of the iterative simulation.

The input data are the electric current and the force as a function of time based on experimental measurement data. The initial force application is solved for $t_{sim} = 1$ s at the beginning. The result is the displacement and the contact

Fig. 5 Image of the sheet surface by optical microscope and scanning electron microscope (SEM)

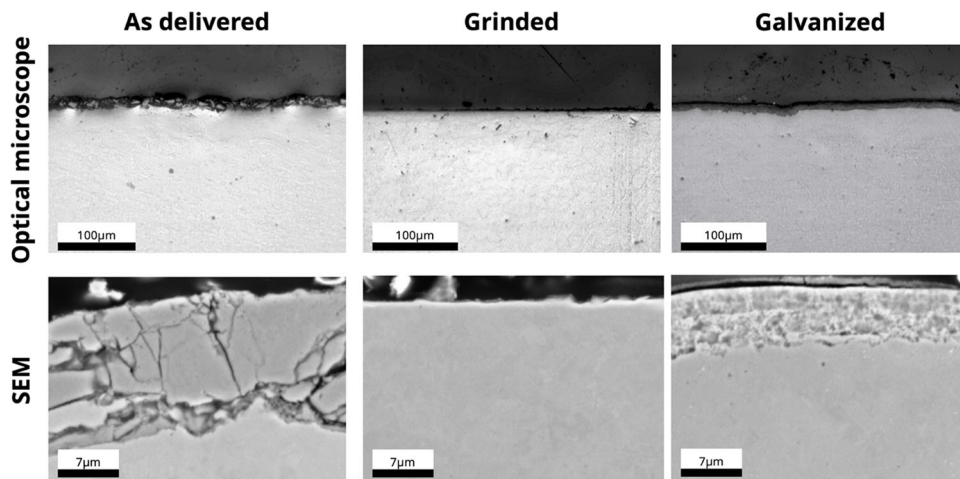
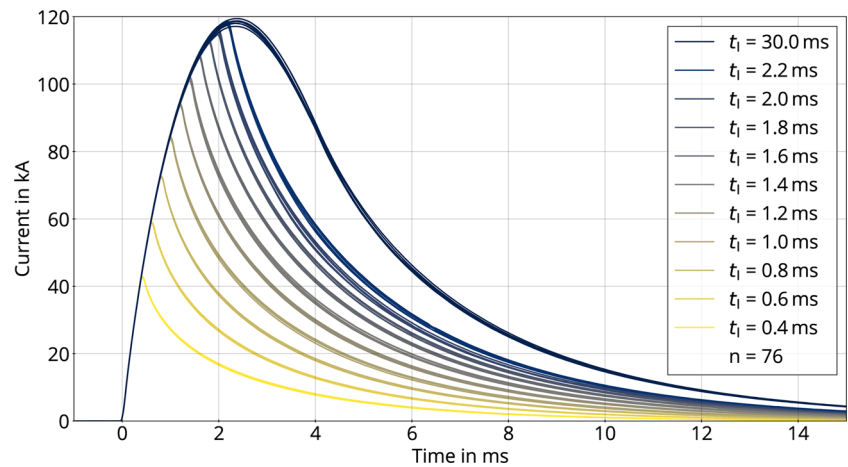


Fig. 6 Current curves of the interruption tests with different interruption times t_I , 7 tests n per interruption test, 1 outlier, surface condition: *as delivered*



pressure σ_C in the joining zone, so that for room temperature T_R the contact resistance R_C according to equation Eq. 5 can be calculated for all contact areas according to Song in [32]. The mechanical-thermal simulation is transferred to an electrical-thermal simulation. The advantage of this is that the mesh geometry and displacement are kept and this does not have to be recalculated. The electrical-thermal simulation is solved for a small time step $\Delta t_{sim} = 0.001$ ms. The solution is a temperature distribution of the deformed geometry. This temperature distribution is transferred to the existing thermal-mechanical simulation. This simulation is then continued. In this way, a temperature-dependent deformation is considered. This procedure is repeated until the end of the simulation time is reached (here $t_{sim} = 1.0024$ s). In this investigation, this is equal to t_p .

$$R_C(T, \sigma_C) = 3\xi \left(\frac{\sigma_s(T)}{\sigma_C^\kappa} \right) \cdot \left(\frac{\rho_1(T) + \rho_2(T)}{2} + \rho_{film} \right) \quad (5)$$

This temperature and contact pressure σ_C dependent contact theory, according to Song, is validated for projection welding of steel alloys [32]. The yield strength σ_s of the soft material, the specific electrical resistances $\rho_{1,2}$ of the joining materials, and a film resistivity ρ_{film} are considered. Two numerical parameters are also considered. According to Song, the numerical parameters ξ and κ describe the surface properties. The contact theory has been validated in this or a similar form in numerous numerical investigations for resistance spot or projection welding [28, 31, 32, 34, 35]. Validation is usually done by comparing the area over melting temperature in the simulation and the area of the solidification microstructure in the experiment (spot weld geometry). As mentioned above, the joint in CD projection welding is not necessarily formed via the molten phase. Therefore the simulation is adapted to the experiment via the transition

voltage of all single contact areas [14, 18]. In the experiment, the transition voltages between Electrode-Projection (EP) U_{EP} , Projection-Sheet (PS) U_{PS} and Sheet-Electrode (SE) U_{SE} are measured. The transition voltages are corrected by subtracting the induced voltage of the CD welding machine [36]. The principle measurement setup is described in [14]. In order to adapt the simulation to the experiment, the numerical parameters ξ and κ from equation Eq. 5 are varied in a time-dependent manner in the numerical process simulation, so that the voltage curve matches the experiment [14]. In Table 1, are listed values of numerical parameters ξ and κ . κ is constant 0.5, according to Song's recommendations [32]. In Fig. 9, is the adjustment of the transition voltage up to the current maximum I_p shown. High simulation times are required because of the permanent adaptive remeshing. Therefore, the simulation is terminated when the current maximum is reached at approx. 2.4 ms.

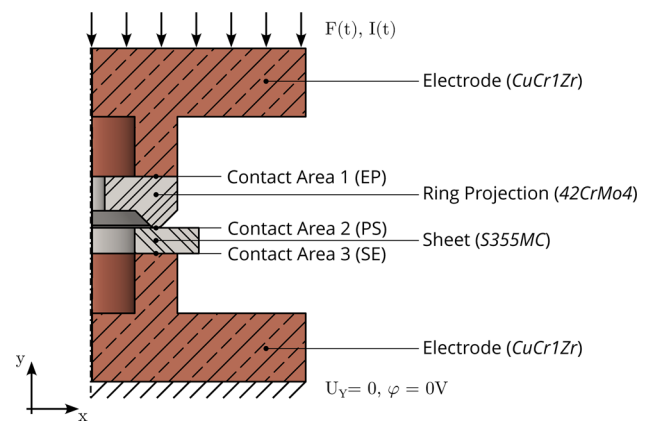


Fig. 7 Schematic 2D axisymmetric representation of the simulation model with the joining parts, electrodes, contact areas, and boundary conditions

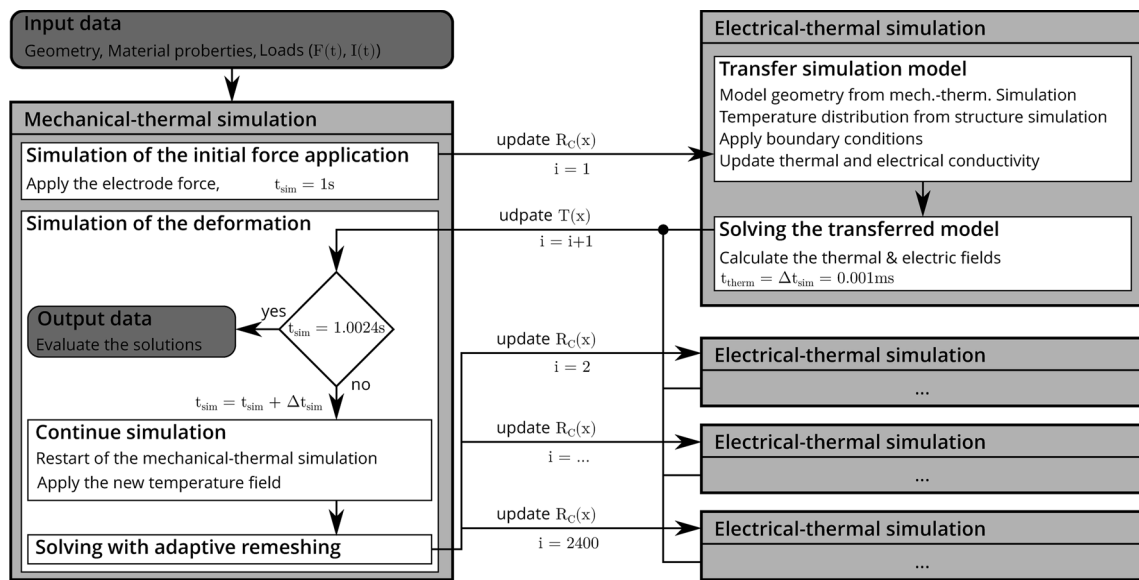


Fig. 8 Procedure of the iterative process simulation for projection welding

4 Results

4.1 Experimental results

4.1.1 Transition resistance

The transition resistance measurement is carried out by a laboratory current source. This is integrated into the welding process so that measurements can be performed before and after welding. For this purpose, the welding circuit of the capacitor discharge is mechanically disconnected automatically during the measurement. The measurement is performed in reference to [37]. The measuring current is 60A and the measuring duration is 15 s. An averaged electrical

voltage of the last 5 s is formed and then the transition resistance is calculated. The results of the transition resistance measurement R_T after welding for the surface condition *As delivered* are shown in Fig. 10. An instantaneous drop of all transition resistances R_T can be observed at an interruption time of $t_I = 0.4$ ms. The behavior is similar for the other surface conditions. The transition resistance R_K before welding for the Electrode-Projection (EP) contact area is $R_{EP} = 48.44 \mu V \pm 0.13 \mu V$. The transition resistance R_K before welding for the Projection-Sheet (PS) contact area is $R_{PS} = 35.13 \mu V \pm 0.16 \mu V$. The transition resistance R_K before welding for the Sheet-Electrode (SE) contact area is $R_{SE} = 79.69 \mu V \pm 0.25 \mu V$. Based on the values before welding, it becomes obvious that a significant drop in the transition resistance already occurs from an interruption time of 0.4 ms. These become smaller with increasing interruption time t_I . Small transition resistances R_T indicate bonded material connections, but at 0.4 ms no material connection was produced for any surface condition. This already indicates the beginning of surface activation, since the interfaces of the joining parts are getting closer and the transition resistance R_T is therefore decreasing.

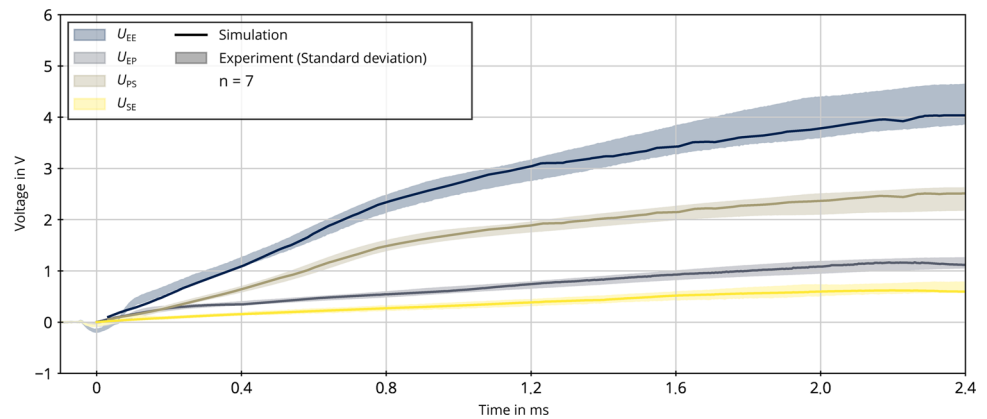
Table 1 Variation of the numerical parameters depending on the contact areas

t in s	κ	ξ_{EP}	ξ_{PS}	ξ_{SE}
0.0002	0.5	220	0.0100	55.0
0.0004	0.5	140	0.1000	55.0
0.0006	0.5	130	2.5000	55.0
0.0008	0.5	120	3.5000	55.0
0.0010	0.5	110	1.0000	57.0
0.0012	0.5	110	0.0030	57.0
0.0014	0.5	105	0.0010	57.0
0.0016	0.5	105	0.0009	65.0
0.0018	0.5	100	0.0006	65.0
0.0020	0.5	95	0.0005	65.0
0.0022	0.5	96	0.0004	69.0
0.0024	0.5	98	0.0004	69.5

4.1.2 Destructive testing

The ring projection is pressed out of the sheet during the press-out tests and the maximum force F_Z is measured. In Fig. 11 the press-out forces F_Z are shown with standard deviation for all interruption times t_I and for the different surface conditions. A maximum force F_Z of approx. 30 kN is determined for all surface conditions. An unacceptable spatter class is determined for the surface condition *As delivered*

Fig. 9 Adjustment of the numerical parameter ξ and κ to adjust the transition voltage in the simulation to the experiment for the number of trials $n = 7$



starting at 2.2 ms according to [7, 14]. This is determined for the surface condition *Grinded* from an interruption time of 1.8 ms and for Galvanized from 1.4 ms. Under consideration of the spatter class, the surface condition *As delivered* reaches the highest press-out force F_Z . The galvanized surfaces reach the lowest maximum press-out force F_Z of approx. 20 kN. A material connection can only be determined from 0.8 ms, irrespective of the surface condition. **At this point, the question is if the material connection was created by a surface activation with metal vaporization. If the material connection is created without metal vaporization, then the activation according to [7, 8] is not necessary for the production of the material connection for short-time welding processes.** To figure this out, the material connections are analyzed by SEM and the power density j_p in the joining zone is determined in the process simulation.

4.1.3 Microstructure

The sheet material is a thermomechanically rolled structural steel S355MC with a fine-grained microstructure. The 42CrMo4 projection component has a ferritic-pearlitic microstructure. The elemental content of manganese, molybdenum and chromium in the projection component (42CrMo4) is higher than in the sheet component (S355MC) in SEM-

EDX images, e.g., by the line scan *L1* from Fig. 12: a normalized mass concentration of 1.11 % manganese in the projection component to 0.22 % in the sheet component was determined. This is an interruption time t_I of 0.8 ms, where the first time a material connection is created. A transition range of the normalized mass concentration of manganese, chromium, or molybdenum can be detected by the line scan *L1* within the joining zone (see Fig. 12). The thickness of the transition area (diffusion zone) is 2 μm to 4 μm and is independent of the surface condition. **This confirms the hypotheses that the material connection is established via the atomic proximity of the activated surfaces and not via the molten phase.** A solidification structure cannot be detected.

Figure 13 shows an SEM-EDX image of the edge area of the joining zone at an interruption time t_I of 0.8 ms. The galvanized sheet surface outside the joining zone can be clearly seen. No zinc can be detected in the center of the joining zone. In the outer area of the joining zone, the zinc surface is melted but not pushed out of the joining zone. A normalized mass concentration of zinc of 1.01 % is detectable at measuring point *M1*. No more zinc is detectable in the outer area starting at t_I of 1.0 ms. **This confirms also the hypotheses that the material connection is established via the atomic proximity of the activated surfaces and not via the molten phase.**

Fig. 10 Transition resistance T_R of the individual contact areas per interruption time for the surface condition: *as delivered*

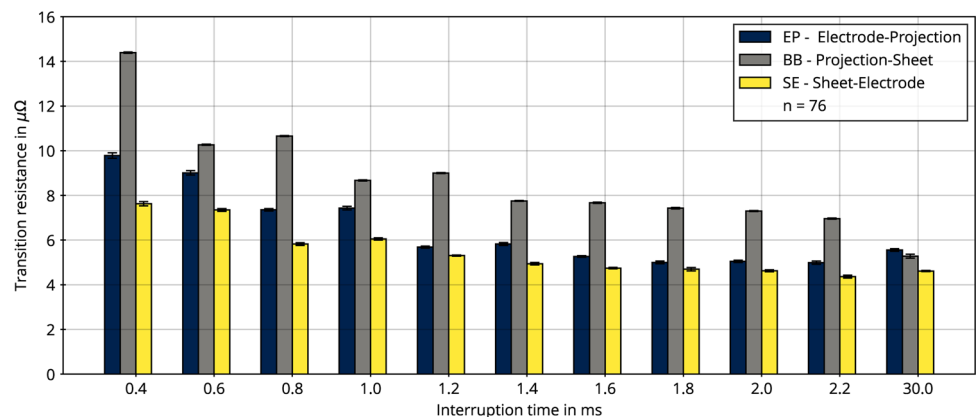
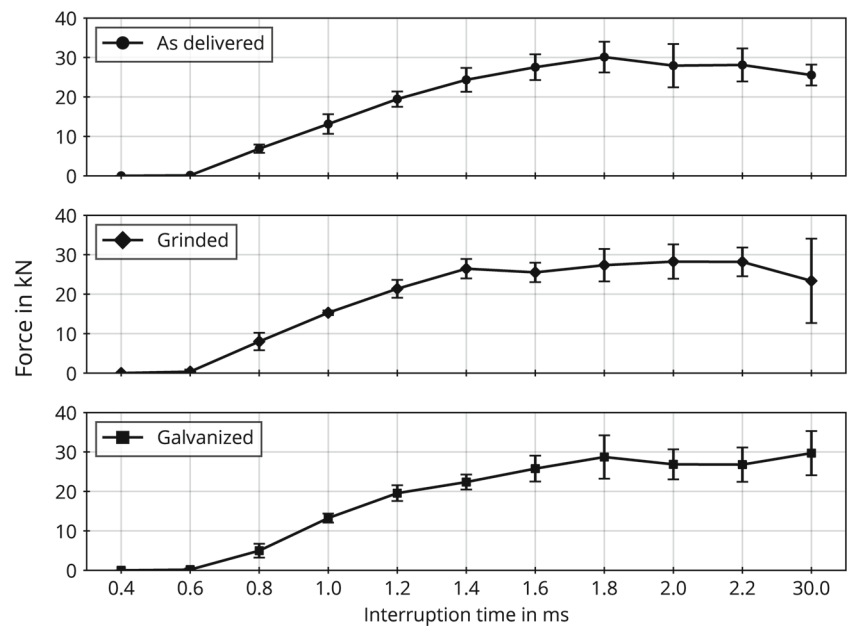


Fig. 11 Static press-out forces F_Z for different interruption times t_I and surface conditions



4.2 Numerical results

The development of the maximum temperature T in the projection cross-section is shown in Fig. 14. The temperature T increases by approx. 50 K within 0.4 ms at the beginning. Almost no deformations of the projection can be observed. The temperature increases more strongly from a simulation time t_{sim} of 0.4 ms. For $t_{sim} = 0.8$ ms, maximum temperatures T of 750 K are observed in the projection cross-section. From $t_{sim} = 0.8$ ms, the temperature T does not increase until 1.0 ms. This is due to the phase transformation, which is considered by the temperature-dependent material data (see specific enthalpy h_V in [14, 18]). After $t_{sim} = 1.0$ ms, the temperature T continues to increase and reaches a maximum of 2020 K at $t_{sim} = 2.25$ ms. The evolution of the temperature distribution

in Fig. 14 shows that the temperature T always increases in the outer region of the projection since the current density j is also the highest here. That's why the projection geometry must be selected in such a way that surface activation in the center of the projection is enabled by a small contact area.

The analysis of the temperature distribution indicates that surface activation starts in the outer area of the contact zone. The power density j_p in the joining zone indicates if metal vapor formation is possible. A differentiation is made in laser beam welding between keyhole and penetration mode welding. An outgoing metal vapor can be seen at the metal surface. The laser beam is reflected several times within the vapor capillary [16]. Power densities j_p between 1 MW/cm² to 5 MW/cm² are necessary to form the metal vapor during laser keyhole welding [15–17]. The maximum current density j

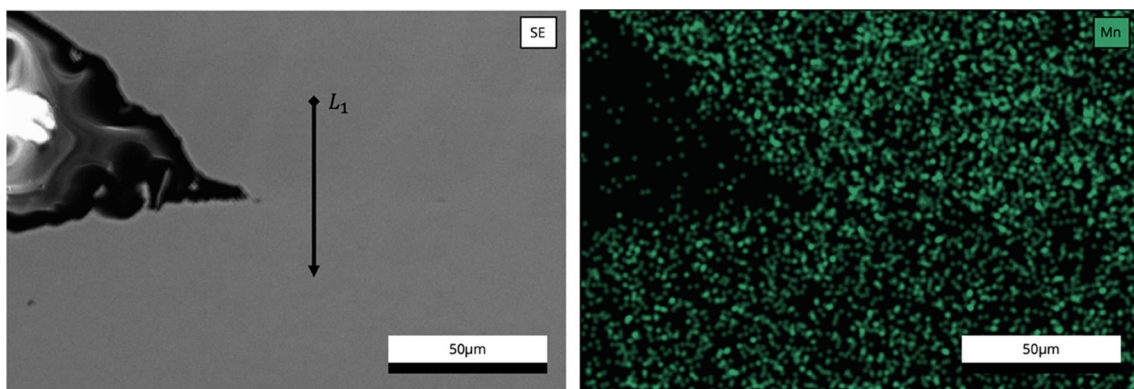


Fig. 12 SEM/EDX of the projection welded joint with surface condition *As delivered* at an interruption time t_I of 0.8 ms. Result from the line scan L_1 : a normalized mass concentration of 1.11% manganese in the projection component to 0.22 % in the sheet component

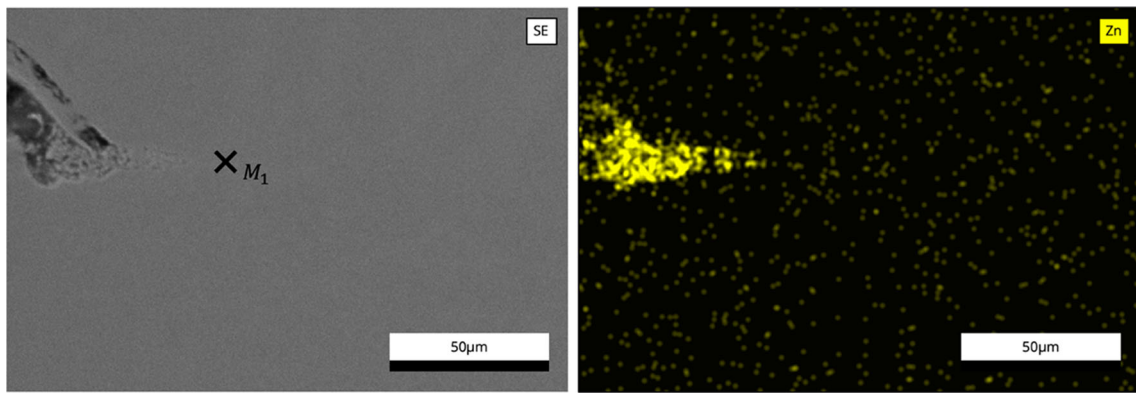


Fig. 13 SEM/EDX of the projection welded joint with the galvanized surface at an interruption time t_I of 0.8 ms. Result from the measuring point M_1 : normalized mass concentration of zinc of 1.01 %

Fig. 14 Development of the maximum temperature and distribution of the numerical process simulation. The temperature distribution in the cross-section is shown at certain points in time

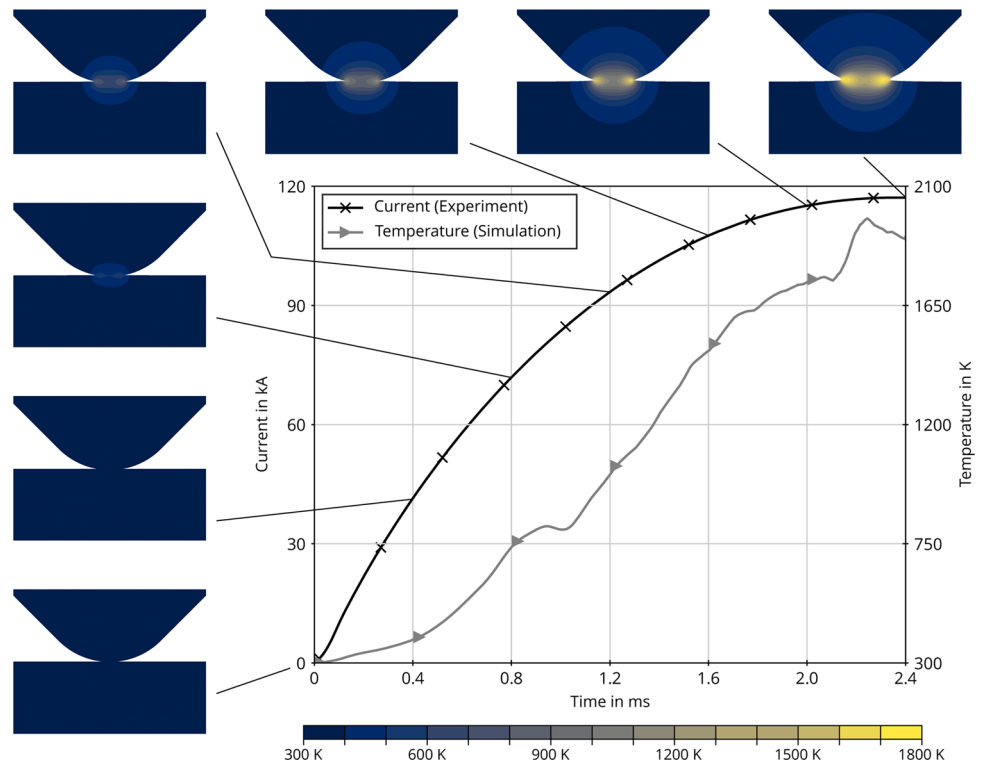
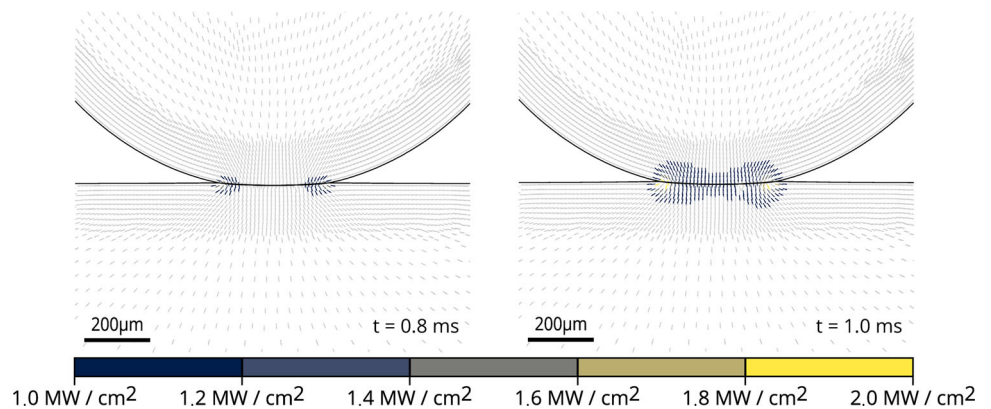


Fig. 15 Distribution of the power density j_p in the joining zone as a function of the simulation time $t_{sim} = 0.8$ ms and 1.0 ms. The power density j_p is only displayed in color from 1.0 MW/cm² and indicates metal vaporization



was multiplied by the voltage drop across the contact area Projection-Sheet (PS) U_{PS} to estimate the maximum power density j_p acting in the joining zone during CD projection welding (see Eq. 6).

$$j_p = j \cdot U_{PS} \quad (6)$$

The distribution of the power density j_p in the joining zone as a function of the simulation time $t_{sim} = 0.8$ ms and 1.0 ms is shown in Fig. 15. The power density j_p is only displayed in color from 1.0 MW/cm² and indicates metal vaporization.

The vaporization starts at the outer edge of the contact area and continues inwards. The power density j_p in the entire contact area reaches values above 1 MW/cm², the limit value for metal vapor formation, from a time of one millisecond [15–17]. **The material connection is created by the formation of metal vapor during CD projection welding.** In the future, the effect of projection geometry, material, and machine characteristics (force generation, resetting, rate of current rise) can be evaluated simulatively.

5 Bonding mechanism in short-time welding

Resistance short-time welding processes are characterized by such high power densities j_p that the material connection is created by the atomic proximity of activated surfaces. The surfaces are activated by metal vapor formation in resistance short-time welding. Power densities j_p higher than 1 MW/cm² are required in the joining zone to form a metal vapor. To achieve a high power density (≥ 1 MW/cm²) for the activation of the surface, very high time gradients are required, which leads to very short welding times. For this reason, these types of resistance welding processes are referred by the term short-time welding. Since short-time welding is defined in terms of time randomly, the description via the physical phenomena is more convenient, e.g., metal vapor welding or sublimation welding. The material connection can be made by metal vapor formation only. With increasing interruption time t_p , this effect is extended by the suppression of the molten phase in the joining zone. This explains why the press-out force F_Z increases and if the power density j_p is too high, heavy weld spatter occurs.

6 Conclusion

The term resistance short-time welding was physically described within the scope of the investigations. Experimental and simulative investigations were performed. Three different surface conditions were considered so that the findings are generally valid (*As delivered, Grinded, Galvanized*). Resistance short-time welding is defined as a process in

which the power density j_p is so high that surfaces are activated by metal vaporization. The material connection is then formed by plastic deformation of areas close to the surface when the parts are pressed together. The material connection is not formed via the molten phase. No solidification structure and therefore no nugget can be detected in the cross-section. Quality requirements should be considered according to the bonding mechanism since no nugget can be measured.

Funding Open Access funding enabled and organized by Projekt DEAL.

Declarations

Conflict of interest The authors declare no competing interests.

Open Access This article is licensed under a Creative Commons Attribution 4.0 International License, which permits use, sharing, adaptation, distribution and reproduction in any medium or format, as long as you give appropriate credit to the original author(s) and the source, provide a link to the Creative Commons licence, and indicate if changes were made. The images or other third party material in this article are included in the article's Creative Commons licence, unless indicated otherwise in a credit line to the material. If material is not included in the article's Creative Commons licence and your intended use is not permitted by statutory regulation or exceeds the permitted use, you will need to obtain permission directly from the copyright holder. To view a copy of this licence, visit <http://creativecommons.org/licenses/by/4.0/>.

References

- Peter NJ, Gerlitzky C, Altin A, Wohletz S, Krieger W, Tran TH, Liebscher CH, Scheu C, Dehm G, Groche P, Erbe A (2019) Atomic level bonding mechanism in steel/aluminum joints produced by cold pressure welding. *Materials* 7:100396. <https://doi.org/10.1016/j.mta.2019.100396>
- Rischka D (1981) Untersuchungen zum Bindemechanismus beim kaltpreßschweißen ausgewählter metalle. Ph.D. Thesis, Technische Universität Dresden, Germany, Dresden
- Pries H (1985) Untersuchung zum Bindungsmechanismus Beim Schweißen Von Metallen Mit Nichtmetallen Im Ultrahochvakuum. 89. Fortschritt-Berichte VDI, VDI-Verlag GmbH, Germany, Dusseldorf
- Bay N (1979) Cold pressure welding-the mechanisms governing bonding. *Journal of Engineering for Industry* 101(2):121–127. <https://doi.org/10.1115/1.3439484>
- Wei Y, Li H, Sun F, Zou J (2019) The interfacial characterization and performance of cu/al-conductive heads processed by explosion welding, cold pressure welding, and solid-liquid casting. *Metals* 9(2):237. <https://doi.org/10.3390/met9020237>
- D'Angelo R, Schur H-J (1971) Untersuchung zum rationellen einatz des kaltpreßschweißens durch plastische deformation und Überlagerung zusätzlicher bewegungskomponenten. Ph.D. Thesis, Technische Universität Dresden, Germany, Dresden
- Ketzel M-M, Hertel M, Zschetzsch J, Füssel U (2019) Heat development of the contact area during capacitor discharge welding. *Welding in the World* 63(5):1195–1203. <https://doi.org/10.1007/s40194-019-00744-x>

8. Zschetzsch J, Ketzler M-M, Füssel U, Rusch H-J, Stocks N (2019) Process monitoring at capacitor discharge welding. In: ASNT Research Symposium 2019 Proceedings, pp. 154–160. ASNT, Orange County. <https://doi.org/10.32548/RS.2019.017>
9. Dattoma, V., Palano, F., Panella, F.W (2010) Mechanical and technological analysis of AISI 304 butt joints welded with capacitor discharge process. *Mater Des* 31(1):176–184. <https://doi.org/10.1016/j.matdes.2009.06.035>
10. Cao X, Zhou Z, Luo J, Zou C, Zou C (2019) Capacitor discharge welding of nuts to steel sheets. *J Mater Process Technol* 264:486–493. <https://doi.org/10.1016/j.matdes.2009.06.035>
11. Lienert TJ, Lear CR, Steckley TE, Lindamood LR, Gould JE, Maloy SA, Eftink BP (2019) Projection-capacitor discharge resistance welding of 430 stainless steel and 14wt. *J Manuf Process* 75:1189–1201. <https://doi.org/10.1016/j.jmapro.2022.01.036>
12. Wehle M (2020) Basics of process physics and joint formation in resistance projection welding processes. Ph.D. Thesis, University Stuttgart, Germany, Stuttgart
13. Maizza, G., Pero, R., De Marco, F., Ohmura, T. (2020): Correlation between the indentation properties and microstructure of dissimilar capacitor discharge welded wc-co/high-speed steel joints. *Materials* 13(11):2657. <https://doi.org/10.1016/j.jmapro.2022.01.036>
14. Koal J, Baumgarten M, Zschetzsch J, Füssel U (2022) Impact of activation in projection welding with capacitor discharge using multiphysics simulation and a process-integrated transition resistance measurement. In: Sommitsch C, Enzinger N, Mayr P (eds) *The 13th international seminar “numerical analysis of weldability”*, vol 13. Publisher of Graz University of Technology, Leibnitz
15. Chen X, Wang H-X (2001) A calculation model for the evaporation recoil pressure in laser material processing. *Journal of Physics D: Applied Physics* 34(17):2637–2642. <https://doi.org/10.1088/0022-3727/34/17/310>
16. Lee JY, Ko SH, Farson DF, Yoo CD (2002) Mechanism of key-hole formation and stability in stationary laser welding. *Journal of Physics D: Applied Physics* 35(13):1570–1576. <https://doi.org/10.1088/0022-3727/35/13/320>
17. Semak V, Matsunawa A (1997) The role of recoil pressure in energy balance during laser materials processing. *Journal of Physics D: Applied Physics* 30(18):2541–2552. <https://doi.org/10.1088/0022-3727/30/18/008>
18. Koal J, Baumgarten M, Heilmann S, Zschetzsch J, Füssel U (2020) Performing an indirect coupled numerical simulation for capacitor discharge welding of aluminium components. *Processes* 8(11):1330. <https://doi.org/10.3390/pr8111330>
19. Hömberg D, Duderstadt F, Dreyer W (2003) Modelling and simulation of capacitor impulse welding. *Mathematics - Key Technology for the Future* 233–242. <https://doi.org/10.1007/978-3-642-55753-8>
20. Duderstadt F, Hömberg D, Khludnev AM (2003-06) A mathematical model for impulse resistance welding: mathematical model for welding. *Math Meth Appl Sci* 26(9):717–737. <https://doi.org/10.1002/mma.372>
21. Casalino G, Panella F (2006-05-01): Numerical simulation of multi-point capacitor discharge welding of AISI 304 bars. *Proceedings of the Institution of Mechanical Engineers, Part B: Journal of Engineering Manufacture* 220(5):647–655. <https://doi.org/10.1243/09544054JEM309>
22. Casalino G, Ludovico AD (2008-02) Finite element simulation of high speed pulse welding of high specific strength metal alloys. *J Mater Process Technol* 197(1):301–305. <https://doi.org/10.1016/j.jmatprotec.2007.06.049>
23. Cavaliere P, Dattoma V, Panella FW (2009-10) Numerical analysis of multipoint CDW welding process on stainless AISI304 steel bars. *Comput Mater Sci* 46(4):1109–1118. <https://doi.org/10.1016/j.commatsci.2009.05.020>
24. Zhu W-F, Lin Z-Q, Lai X-M, Luo A-H (2006) Numerical analysis of projection welding on auto-body sheet metal using a coupled finite element method. *Int J Adv Manuf Technol* 28(1):45–52. <https://doi.org/10.1007/s00170-004-2336-8>
25. Sun X (2000) Modeling of projection welding processes using coupled finite element analyses. *Weld J* 244–251
26. Afzal A, Hamedi M, Nielsen CV (2021) Numerical and experimental study of ALSI coating effect on nugget size growth in resistance spot welding of hot-stamped boron steels. *J Manuf Mater Process* 5(1):1–13. <https://doi.org/10.3390/jmmp5010010>
27. Deng L, Li Y, Cai W, Haselhuhn AS, Carlson BE (2020) Simulating thermoelectric effect and its impact on asymmetric weld nugget growth in aluminum resistance spot welding. *J Manuf Sci Eng* 142(9):091001. <https://doi.org/10.1115/1.4047243>
28. Tuchtfeld M, Heilmann S, Füssel U, Jüttner S (2019) Comparing the effect of electrode geometry on resistance spot welding of aluminum alloys between experimental results and numerical simulation. *Welding in the World* 63(2):527–540. <https://doi.org/10.1007/s40194-018-00683-z>
29. Li M (1997) Modeling of contact resistance during resistance spot welding. Special publication (NIST SP). National Institute of Standards and Technology, United States of America, Gaithersburg, pp 423–434
30. Long FX. Development of a re-meshing method for the finite-element simulation of a capacitor discharge press-fit welding process. Bachelor Thesis, University of Applied Sciences, Germany, Karlsruhe
31. Hamedi, M., Atashparva, M (2017) A review of electrical contact resistance modeling in resistance spot welding. *Welding in the World* 61(2), 269–290. <https://doi.org/10.1007/s40194-016-0419-4>
32. Song Q (2003) Testing and modeling of contact problems in resistance welding. Ph.D. Thesis, Technical University of Denmark, Denmark, Lyngby
33. Koal J, Baumgarten M, Zschetzsch J, Füssel U (2021) Numerische simulation großer deformationen beim buckelschweißen durch kondensatorentladung. In: *DVS Congress 2021 – Große Schweißtechnische Tagung. DVS-Berichte*, vol. 371, pp. 562–567. DVS Media GmbH, Germany, Dusseldorf
34. Wang J, Wang H-P, Lu F, Carlson BE, Sigler DR (2015) Analysis of Al-steel resistance spot welding process by developing a fully coupled multi-physics simulation model. *International Journal of Heat and Mass Transfer* 89. <https://doi.org/10.1016/j.ijheatmasstransfer.2015.05.086>
35. Wan Z, Wang H-P, Wang M, Carlson BE, Sigler DR. Numerical simulation of resistance spot welding of al to zinc-coated steel with improved representation of contact interactions. *International Journal of Heat and Mass Transfer* 101:749–763. <https://doi.org/10.1016/j.ijheatmasstransfer.2016.05.023>
36. Ketzler M-M, Zschetzsch J, Füssel U (2017) Elimination of voltage measuring errors as a consequence of high variable currents in resistance welding. *Welding and Cutting* 16(3):164–168
37. ISO 18594:2007 – Resistance spot-, projection- and seam-welding – method for determining the transition resistance on aluminium and steel material (2007)

Publisher's Note Springer Nature remains neutral with regard to jurisdictional claims in published maps and institutional affiliations.